CSMA 2026
17ème Colloque National en Calcul des Structures
18-22 Mai 2026, Presqu'île de Giens (Var)

Integrated Projection-enhanced DVC to monitor nonlinearities associated with fracture experiments

M. Valmalle[1], C. Jailin[1], F. Hild[1]

[1] *Université Paris-Saclay, CentraleSupélec, ENS Paris-Saclay, CNRS*
LMPS - Laboratoire de Mécanique Paris-Saclay, 91190 Gif-sur-Yvette, France.
Email: [malo.valmalle, clement.jailin, francois.hild]@ens-paris-saclay.fr

Abstract — Digital Volume Correlation (DVC) is an established method for extracting full-field displacements from *in-situ* experiments monitored by X-ray computed tomography. However, the temporal sampling of such measurements is usually sparse, which limits the analysis of nonlinear phenomena such as plasticity, damage and failure. The method proposed herein consists in enriching the temporal sampling with projections acquired during loading of an *in-situ* cracking experiment. By combining an integrated DVC formulation with a reduced-order Projection-enhanced DVC, it becomes possible to identify the nonlinear evolution of the crack-front, the mode I stress intensity factor, and the associated displacement fields throughout the experiment.
Mots clés — Digital Volume Correlation (DVC), Linear Elastic Fracture Mechanics, Projections.

1 Introduction

Background Additive manufacturing (AM) allows for the fabrication of parts with complex geometries and tailored mechanical properties. In the particular case of Fused Deposition Modeling (FDM), the process in itself may yield anisotropic fracture properties depending on the printing strategy (Figure 1(a)). The study presented herein was conducted using a Compact Tension (CT) specimen of size $50 \times 48 \times 10$ mm^3 made of polycarbonate and printed with an infill of 50% (Figure 1(b)).

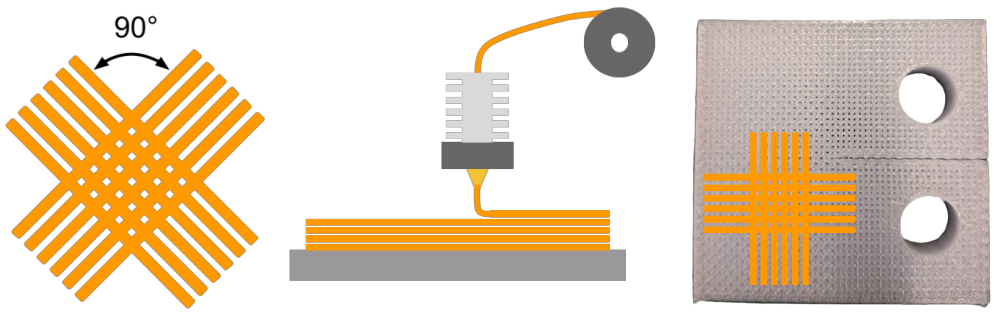

(a) (b)

Figure 1: (a) Schematic view of the FDM process. (b) 3D printed polycarbonate sample with the infill pattern displayed in orange lines.

X-ray computed tomography X-ray Computed Tomography (X-CT) is commonly used to characterize AM materials, as it allows defects induced by the fabrication process (voids, lack-of-fusion regions, filament interfaces) to be visualized in three dimensions. In addition, when combined with loading devices, X-CT enables full-field measurements to be performed in *in-situ* mechanical tests (*i.e.,* mechanical tests monitored by repeated tomographic acquisitions). Such 4D experiments provide access to the evolving microstructure and to the associated kinematic fields, which is of particular interest in the context of damage and fracture of heterogeneous materials [1].

Tomography consists in reconstructing a 3D volume $f(\boldsymbol{x})$ for all space locations $\boldsymbol{x}$ from sets of radiographs $p(\boldsymbol{\xi}, \Theta)$ acquired on the detector coordinates $\boldsymbol{\xi}$ at various angles Θ. The reconstruction is

performed by minimizing

$$\Gamma_{\text{recon}} = \sum_{\boldsymbol{\xi},\Theta} \|\Pi_\Theta[f(\bullet)](\boldsymbol{\xi}) - p(\boldsymbol{\xi},\Theta)\|^2, \tag{1}$$

where Π_Θ is the projection operator that maps the 3D volume $f(\boldsymbol{x})$ onto the detector plane for a given angle Θ. The cost function Γ_{recon} is minimized using the Simultaneous Iterative Reconstruction Technique (SIRT) from Astra toolbox [2].

***In-situ* fracture experiment** An *in-situ* fracture experiment was carried out on the CT specimen displayed in Figure 1(b), using a loading device mounted inside the tomograph, as shown in Figure 2(a). The corresponding force vs. displacement curve is displayed in Figure 2(b). Two initial tomographic acquisitions were performed for uncertainty quantification and five scans were acquired for deformed configurations after subsequent loading steps of 1 mm. Between these scans, X-ray projections were continuously acquired during the load ramps, at a fixed angle $\Theta = 0°$. These projections, which are usually discarded once the CT reconstructions are performed, are here exploited to enrich the temporal sampling of the kinematic measurements.

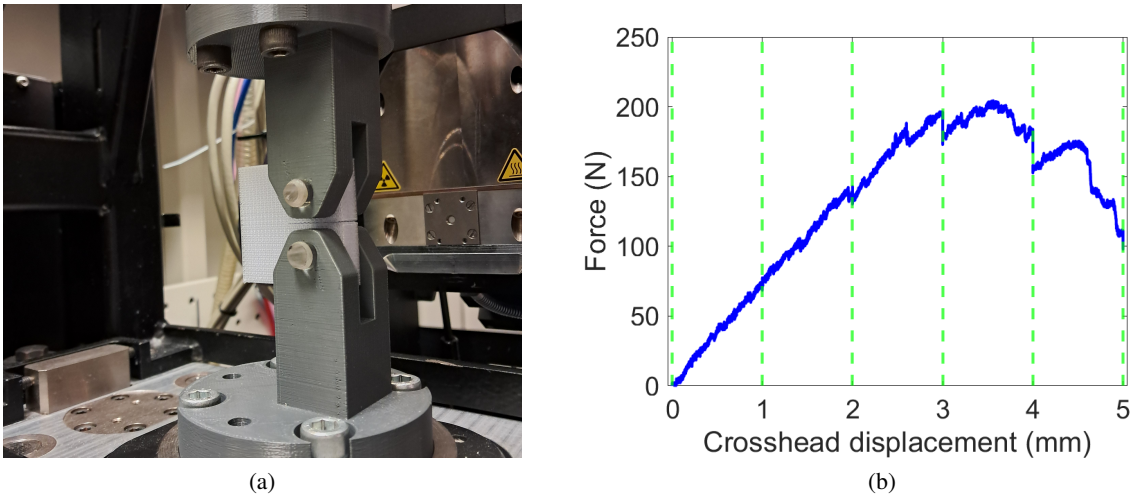

(a) (b)

Figure 2: (a) In-situ experimental setup. (b) Force vs. displacement curve (the green dashed lines depict tomographic acquisitions).

2 Methods

Integrated DVC Digital Volume Correlation (DVC) was used to measure the displacement fields for the different scans. As for Digital Image Correlation [3], there are essentially two types of approaches to measure volumetric displacements, namely, local DVC in which small and independent sub-volumes are registered [4] and global (or FE-based) DVC [5] for which the whole region of interest is meshed and correlated in a single analysis. Both of these approaches are measuring a displacement field between the reference volume $f(\boldsymbol{x})$ and a sequence of deformed volumes $g(\boldsymbol{x},T)$, acquired for turn T, with the space/time displacement field $\boldsymbol{u}(\boldsymbol{x},T)$ (Figure 3) such that

$$\Gamma_{\text{DVC}} = \sum_{\boldsymbol{x}} \|f(\boldsymbol{x}+\boldsymbol{u}(\boldsymbol{x},T)) - g(\boldsymbol{x},T)\|^2, \quad \text{with} \quad u_{\text{sol}} = \arg\min \Gamma_{\text{DVC}}. \tag{2}$$

The kinematic basis is then to be chosen depending on the the mechanical problem, for instance, rigid body motions or finite element shape functions may be used. In the context of fracture mechanics, however, strain and stress fields exhibit square-root singularities and specific angular variations near crack tips. To account for these features in a compact and mechanically meaningful way, an integrated DVC approach [6] is adopted in which the displacement field is expressed in terms of Williams' series [7]. The fields $\boldsymbol{\varphi}_n^I$, $\boldsymbol{\varphi}_n^{II}$ and $\boldsymbol{\varphi}_n^{III}$ correspond to the asymptotic solutions of an infinite elastic body containing a semi-infinite crack along the x-axis ($x < 0$), for modes I, II and III, respectively. For each plane of the

mesh, the displacement field is written as

$$\mathbf{u}(\mathbf{z}) = \sum_{j=I}^{III} \sum_{n=n_{\min}}^{n_{\max}} a_n^j \boldsymbol{\varphi}_n^j(\mathbf{z}) \quad \text{for each plane of the mesh,} \tag{3}$$

where $\boldsymbol{z} = (r, \theta)$ denotes the local polar coordinates of a current point measured from the crack tip, and a_n^j are the unknown amplitudes of the different Williams' modes

$$\begin{aligned}
\boldsymbol{\varphi}_n^I(r,\theta) &= \frac{r^{n/2}}{2\mu\sqrt{2\pi}} \left[\kappa \exp\left(\frac{in}{2}\theta\right) - \frac{n}{2}\exp\left(\frac{i(4-n)}{2}\theta\right) + \left((-1)^n + \frac{n}{2}\right)\exp\left(-\frac{in}{2}\theta\right)\right] \\
\boldsymbol{\varphi}_n^{II}(r,\theta) &= \frac{ir^{n/2}}{2\mu\sqrt{2\pi}} \left[\kappa \exp\left(\frac{in}{2}\theta\right) + \frac{n}{2}\exp\left(\frac{i(4-n)}{2}\theta\right) + \left((-1)^n - \frac{n}{2}\right)\exp\left(-\frac{in}{2}\theta\right)\right] \\
\boldsymbol{\varphi}_n^{III}(r,\theta) &= \frac{2r^{n/2}}{\mu\sqrt{2\pi}} \sin\left(\frac{n}{2}\theta + \frac{1+(-1)^n}{2}\frac{\pi}{2}\right)
\end{aligned} \tag{4}$$

with $\kappa = (3-4\nu)$, where Kolossov's constant κ is expressed under plane strain condition, with ν the Poisson's ratio of the material, and μ the shear modulus. The role of the various terms is briefly recalled. For $n = 1$, the fields correspond to the singular strain / stress fields generated by presence of the crack whose amplitudes a_1^j will give access to the Stress Intensity Factors (SIF) for modes I, II and III. For $n = 2$, and $j = I$ the amplitude a_2^I corresponds to a uniform stress, the so-called "T-stress" (uniaxial tension along the crack direction). Higher order (*i.e.,* subsingular) terms allow the effect of the boundary conditions to be captured. Supersingular terms (*i.e.,* $n < 0$) induce diverging strain energies at the crack-front, and are usually discarded except for the first one ($n = -1$) that is used to position the crack-front by canceling out the corresponding amplitudes [8].

The mesh used for the integrated DVC analyses is a cylindrical region around the crack-front, discretized into a finite number of planes along the specimen thickness. On each plane, the displacement field is described by the truncated Williams' expansion (3). This choice provides both a physically consistent description of the near-tip fields and a relatively low number of degrees of freedom compared to generic FE-based DVC.

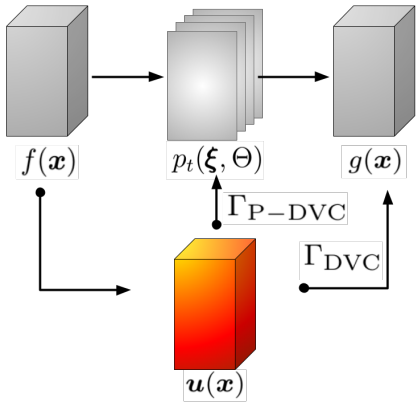

Figure 3: Schematic representation of the volume in the reference configuration $f(\boldsymbol{x})$ to be registered with either the volume in a deformed configuration $g(\boldsymbol{x})$ or projections $p_t(\boldsymbol{\xi}, \Theta)$ acquired on the fly during loading.

Projection-based DVC Integrated DVC analyses provide spatially detailed information on the fracture process, but only at the discrete times corresponding to tomographic scans. Between two scans, the mechanical response may exhibit rich transient behavior (crack arrest and re-propagation, interactions with the printed architecture) that remains unresolved if one only relies on volumetric reconstructions.

To enrich the temporal sampling, one may use Projection-enhanced DVC [9] that consists in registering 2D projections $p_t(\boldsymbol{\xi}, \Theta)$ acquired at different instants of time t during loading steps (Figure 3). The general principle is to minimize the residual between the projected deformed volume and the acquired

projection such that

$$\Gamma_{\text{P-DVC}} = \sum_{\boldsymbol{\xi}} \|\Pi_{\Theta}[f_u(\bullet)](\boldsymbol{\xi}) - p_t(\boldsymbol{\xi},\Theta)\|^2, \quad \text{with} \quad f_u = f(\boldsymbol{x}+\boldsymbol{u}(\boldsymbol{x},t)), \tag{5}$$

where $\boldsymbol{u}(\boldsymbol{x},t)$ denotes the displacement field for time t. It is important to distinguish here the discrete scan turn T used in Equation (2) for tomographic volumes from the projection index t used in Equation (5). The former labels a small number of fully reconstructed 3D images, whereas the latter labels a much larger number of 2D projections acquired between scans. The projection-based registration is costlier computationally and more ill-posed than DVC (which is already computationally intensive and ill-posed). Even though Williams' fields chosen for integrated DVC have less Degrees of Freedom (DoFs) compared to FE-based DVC, they still are too numerous for P-DVC calculations. As such, a reduced basis is selected in the sequel for those calculations.

3 Results

Integrated DVC The integrated DVC analyses are first used to determine appropriate truncation orders in the Williams' expansion, and to quantify the crack-front evolution at scan turns. A "Pacman" mesh composed of 8 layers along the specimen thickness is considered. For each layer (plane), the amplitudes of Williams' fields are to be determined. Direct calculations were performed (*i.e.,* registering the deformed configurations directly with the reference one) on the five deformed volumes using different truncated orders (n_{min} was set to -1 in order to locate the crack-front for each plane (with a convergence criterion of less than one voxel of crack-front offset) and n_{max} ranged from 3 to 11). It is observed that the gray-level residuals decrease when n_{max} increases up to $n_{\text{max}} = 7$, and then reaches a plateau. This result indicates that the additional degrees of freedom introduced for higher order terms do not improve the correlation significantly. A similar convergence behavior is observed for the mode I SIF K_I, whose value stabilizes for $n_{\text{max}} = 7$. The convergence results on the quantity to be minimized in the cost function Γ_{DVC} (*i.e.,* the global gray level residuals) and the mechanical quantity of interest for LEFM (*i.e., K_I*) are thus indicating that $n_{\text{min}} = -1$ and $n_{\text{max}} = 7$ for the truncation are a good compromise.

With this selected truncation, the results are analyzed plane by plane. The change of the crack-front position and mode I SIF for the 5 different scans are displayed in Figure 4. The crack essentially propagated between scan #3 (in yellow) and scan #5 (in green), which is confirmed by the values of K_I that are essentially reaching a plateau after scan #3 (in yellow).

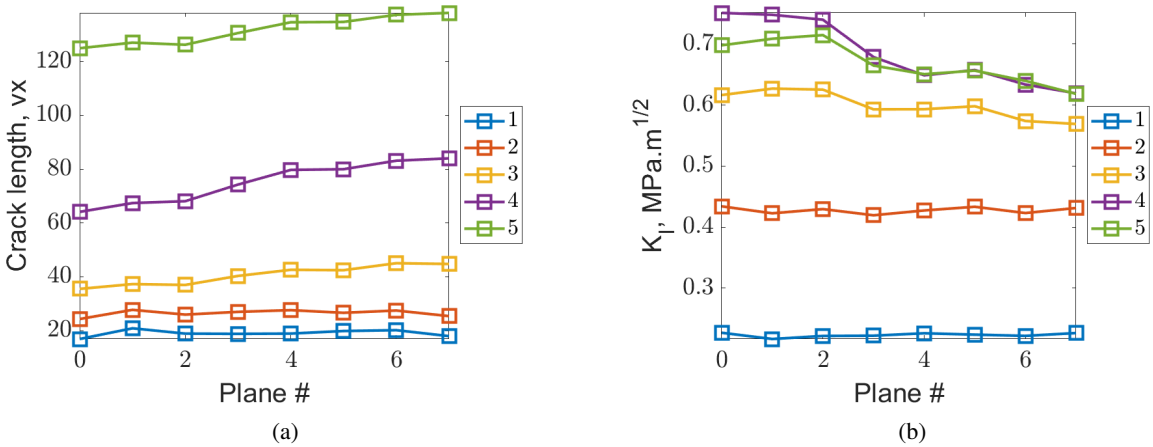

(a) (b)

Figure 4: (a) Crack length (expressed in voxels) for the 5 analyzed scans depending on the plane of the mesh. (b) Mode I SIF profiles for the 5 analyzed scans.

Reduced basis construction Integrated DVC runs give access to spatially detailed information about the fracture process, but it comes at the expense of poor temporal sampling. To get a better temporal sampling, the projections acquired during loading are analyzed using projection-based DVC [9]. To deal with the ill-posedness of the problem and to mitigate the computational cost, a reduced order model

is constructed. To keep a mechanical interpretation of the identified modes, the reduced model is constructed with Williams' fields and not with a pure data reduction (*i.e.,* singular value decomposition) of the I-DVC fields for instance. This approach is once again "integrated" because it is derived from mechanical knowledge about the fracture mechanics fields.

Figure 5(a) shows that the first four mode I amplitudes are predominant throughout the different scans, for $n \in [\![0\ ;\ 4]\!]$. Moreover, it is observed that there is a strong temporal correlation between a_0^I and a_3^I, as well as between a_1^I and a_2^I with Pearson coefficients in excess of 0.97. Those two pairs of modes are assembled to get a "loading related mode" including rigid body motion (RBM) as well as a higher order ($n = 3$) term accounting for a subsingular mode, and an "SIF related mode" including the SIF itself as well as the T-stress. Regarding the amplitudes for mode II (Figure 5(b)), the only field that is needed is $\boldsymbol{\varphi}_0^{II}$ (rigid body motion). Since the measured amplitude of displacements in the out-of-plane direction were very small (*i.e.,* less than 0.7 vx at maximum load), all the fields associated with mode III kinematics were discarded.

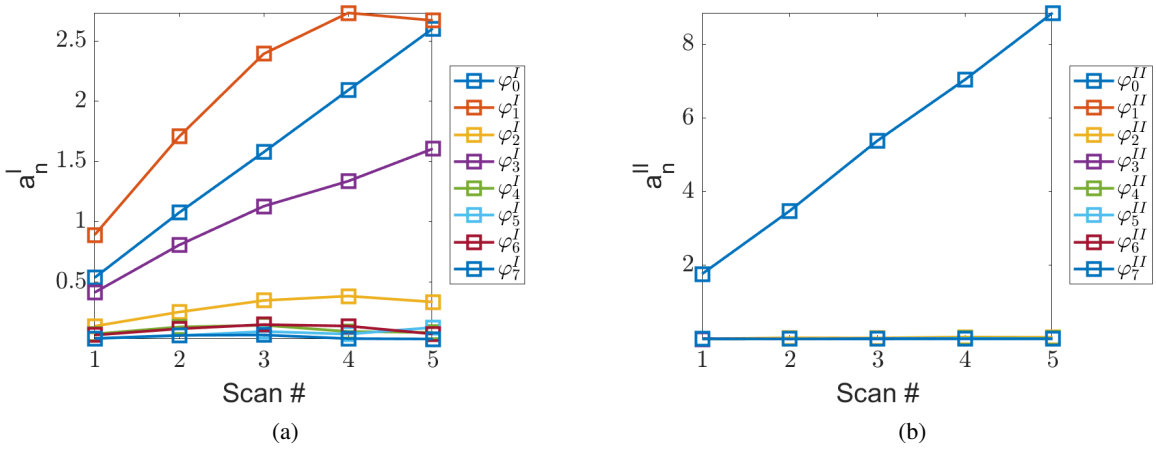

Figure 5: (a) History of mean mode I amplitudes found via I-DVC for the 5 analyzed scans. (b) Corresponding results for mode II amplitudes.

In addition to these modes, an accurate description of the crack-front position is required for each projection. A global supersingular mode $\boldsymbol{\psi}_{-1}$ is built and a global increment of crack-front motion is applied to a crack-front position found via I-DVC (with a convergence criterion of less than one voxel for the absolute crack-front offset). The final set of modes for the reduced basis is gathered in Table 1. It consists of four vector fields, namely, one associated with the crack-front motion, two with rigid body motions (in modes I and II), and one with mode I fracture parameters (SIF and T-stress).

Table 1: Four fields used as a reduced basis and the Williams' fields they include.

Reduced basis mode	$\boldsymbol{\psi}_{-1}$	$\boldsymbol{\psi}_{RBM-I}$	$\boldsymbol{\psi}_{RBM-II}$	$\boldsymbol{\psi}_{SIF-I}$
Williams' fields	$\boldsymbol{\varphi}_{-1}^I$	$\boldsymbol{\varphi}_0^I$ and $\boldsymbol{\varphi}_3^I$	$\boldsymbol{\varphi}_0^{II}$	$\boldsymbol{\varphi}_1^I$ and $\boldsymbol{\varphi}_2^I$

Integrated Projection-based DVC The Integrated Projection-based DVC calculations were run as follows for the last loading step where crack propagation was at play, namely, from scans #4 to #5. For this interval, the crack-front position determined by I-DVC at for scan #4 was used as the initial guess. The reduced basis described previously was constructed from the corresponding Williams fields. For each projection, the crack-front position was found with the global supersingular mode $\boldsymbol{\psi}_{-1}$, and the amplitudes of the other reduced basis modes were measured. This procedure means that it is assumed that the crack-front morphology is the same during the loading step, which is not totally true (Figure 4(a)), but it allows one to check whether the mean crack-front position and displacement fields are consistent with I-DVC results for the subsequent scan.

For the analyzed load step, about 300 projections were acquired and analyzed, which corresponds to an improvement by more than two orders of magnitude in temporal resolution compared to the number of available tomographic scans. As for I-DVC, the convergence criterion on the absolute crack-front offset

was set to one voxel. The convergence criterion of the nested Gauss-Newton (GN) algorithm minimizing $\Gamma_{\text{P-DVC}}$ (Equation (5)) was set to 10^{-2} vx for the RMS amplitude corrections of the fields $\boldsymbol{\psi}$. Three iterations were typically needed to locate the crack front for an increment of propagation larger than 1 vx, and the nested GN algorithm converged in less than 10 iterations for all calculations (because of small amplitude increments between subsequent projections).

The first and last analyzed projections, their corresponding initial (with no displacement correction) and converged residuals are displayed in Figure 6. The initial residuals, which correspond to the raw projection difference with no applied displacement, are high (Figure 6(b,e)). The printing pattern as well as the projected crack front are clearly visible. Moreover, crack propagation is discernible in both residuals. Figure 6(c,f) shows that the level of the residuals at convergence are very low, thereby giving confidence in the results. One can also visualize the displacement of the pacman-mesh found by the procedure as the crack propagated by about 60 vx between those two projections.

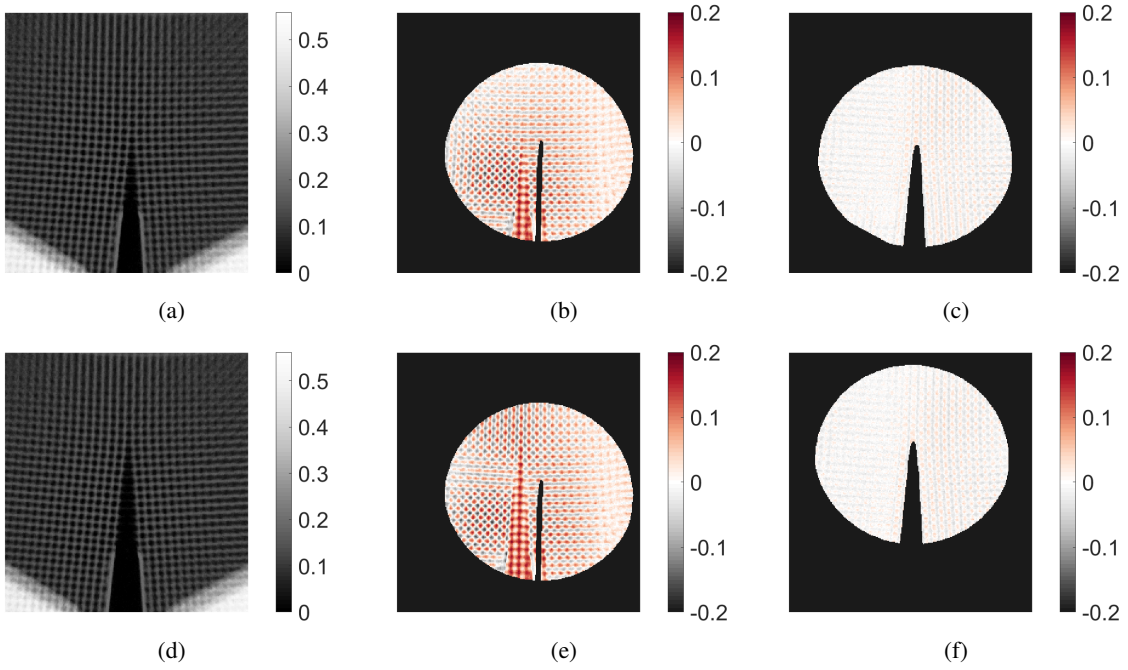

Figure 6: (a) First projection of the analysis. (b) Initial residual for the first projection. (c) Residual at convergence for the first projection. (d) Last projection of the analysis. (e) Initial residual for the last projection. (f) Residual at convergence for the last projection.

The crack-front positions found using this procedure for the final loading step are shown in Figure 7(a). The procedure extracted a consistent crack-front position with respect to that found via I-DVC (for scan #5), although there is a small RMS difference of 4.9 vx to be linked with model error due to the assumption that the crack-front morphology is same during each loading step. Figure 7(b) displays the mean crack length for all P-DVC calculations with force and displacement measurements laid over with arbitrary units. The associated uncertainty computed as the standard deviation of crack length for constant stroke prior to the loading phase is equal to 0.15 vx, which is remarkably low. The drops in force are perfectly matching fast crack propagation events, thus giving confidence in the reported results. It is worth noting that the final drop in force after the prescribed displacement was set (*i.e.,* from increment 246 on) is attributed to crack propagation still occurring after the end of the loading step.

Figure 7(c) shows the mean mode I SIF K_I for all P-DVC calculations. The associated uncertainty computed as the standard deviation of K_I for a constant stroke prior to the loading phase is of the order of 10^{-3} MPa$\sqrt{\text{m}}$, which is 3 orders of magnitude lower than the values reached herein. The mode I SIF levels are steadily rising at the beginning of loading until fast crack propagation events (seen previously) arose. It is worth noting that K_I was not constant during propagation. This fluctuation is attributed to the fact that this loading step was performed in a specimen with a crack that already propagated significantly. As for the previous observations, the main drops in force are perfectly matching drops in K_I levels. The sudden drops in force are to be linked to sudden crack propagation through a complete "unit cell" of

the printing pattern. Those drops in force correspond to sudden crack advance of about 8 vx, which translates into 0.8 mm that is the characteristic length of the printing pattern (the filament was deposited with a 0.4 mm width and with a 50% infill the same width was left unfilled before printing again).

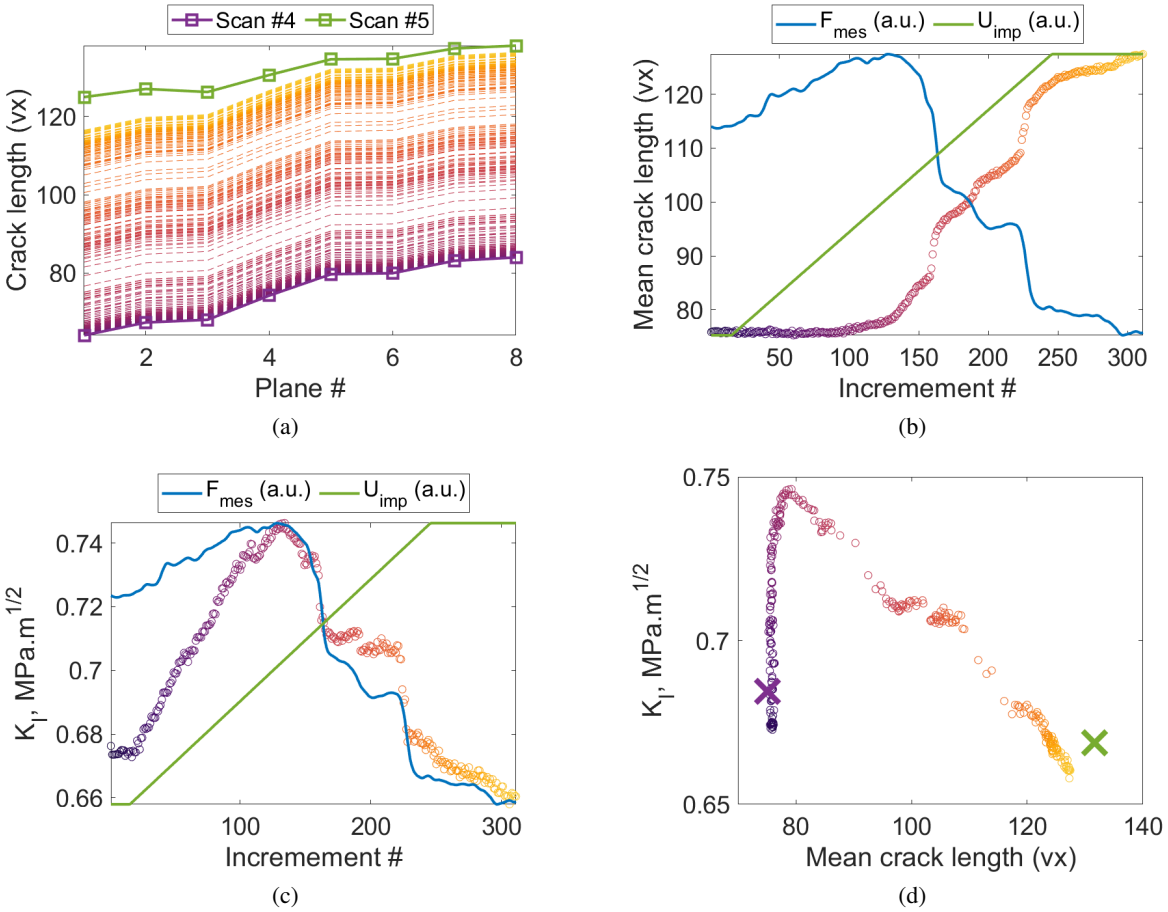

Figure 7: (a) Crack length found via P-DVC for the projections acquired during the final load step (dashed lines with color hues representing time), and compared to I-DVC crack-fronts in solid lines. (b) Mean crack length and (c) mean mode I SIF K_I for all the P-DVC calculations (color hues representing time) in addition to force and displacement measurements displayed with arbitrary units. (d) Mean mode I SIF K_I as a function of mean crack length (I-DVC results for scans #4 and #5 are depicted with crosses).

The history of mean crack length vs. mean mode I SIF K_I is reported in Figure 7(d). The I-DVC results for scans #4 and #5 are also displayed (crosses) for comparison purposes. The cracking response of the studied material during this loading increment is complex, alternating a steady front position (for which the force and SIF vary in a quasi linear manner) at the beginning of loading, followed by discrete depinning-pinning steps. Remarkably, each propagation step is accompanied by a quasi constant SIF level, even though these levels change for each of them. Without P-DVC, it would not have been possible to capture this complex behavior as well as the fact that values of K_I were greater (by about 15%) during this loading step than those measured via I-DVC.

4 Conclusion

A proof of concept of projection-enhanced DVC has been presented when applied to an *in-situ* fracture experiment. The proposed framework combined integrated DVC with a mechanically informed reduced-order basis in order to exploit projections acquired on the fly during loading steps between tomographic scans. The 3D displacement fields, crack-front locations and mode I SIFs were successfully measured using those projections. The measurements were carried out on a mechanics-informed and reduced basis via integrated projection-enhanced DVC.

The approach has been demonstrated on a 3D-printed polycarbonate CT specimen produced by FDM. Approximately 300 projections have been analyzed between each standard DVC loading step. The P-DVC results revealed a complex cracking response involving alternating phases of energy storage at nearly fixed crack length and rapid propagation events at nearly constant K_I, with propagation increments that were comparable to the characteristic length of the printing pattern. Such information is of direct interest for understanding the interplay between fracture mechanisms and the mesostructure of additively manufactured materials.

References

[1] F. Hild, A. Bouterf, and S. Roux. Damage Measurements via DIC. *International Journal of Fracture*, 191(1-2):77–105, 2015.

[2] W. van Aarle, W.J. Palenstijn, J. Cant, E. Janssens, F. Bleichrodt, A. Dabravolski, J. De Beenhouwer, K.J. Batenburg, and J. Sijbers. Fast and flexible X-ray tomography using the ASTRA toolbox. *Optics Express*, 24(22):25129–25147, Oct 2016.

[3] M.A. Sutton. Computer vision-based, noncontacting deformation measurements in mechanics: A generational transformation. *Applied Mechanics Reviews*, 65(AMR-13-1009):050802, 2013.

[4] B.K. Bay, T.S. Smith, D.P. Fyhrie, and M. Saad. Digital volume correlation: three-dimensional strain mapping using X-ray tomography. *Experimental Mechanics*, 39:217–226, 1999.

[5] S. Roux, F. Hild, P. Viot, and D. Bernard. Three dimensional image correlation from X-Ray computed tomography of solid foam. *Composites Part A: Applied Science and Manufacturing*, 39(8):1253–1265, 2008.

[6] S. Roux and F. Hild. Stress intensity factor measurements from digital image correlation: post-processing and integrated approaches. *International Journal of Fracture*, 140(1-4):141–157, 2006.

[7] M. L. Williams. On the stress distribution at the base of a stationary crack. *Journal of Applied Mechanics*, 24(1):109–114, 03 1957.

[8] S. Roux, J. Réthoré, and F. Hild. Digital Image Correlation and Fracture: An Advanced Technique for Estimating Stress Intensity Factors of 2D and 3D Cracks. *Journal of Physics D: Applied Physics: Appl. Phys.*, 42:214004, 2009.

[9] V. Kosin, A. Fau, C. Jailin, B. Smaniotto, T. Wick, and F. Hild. A projection-based approach to extend digital volume correlation for 4D spacetime measurements. *Comptes Rendus. Mécanique*, 351:265–280, 2023.